Superimposed wavefront imaging of diffraction-enhanced x-rays: A method to achieve higher resolution in crystal analyzer-based x-ray phase-contrast imaging 🄢 🄕 ⊘

Naoki Sunaguchi ✉ 📵 ; Tetsuya Yuasa 📵 ; Daisuke Shimao 📵 ; Shu Ichihara 📵 ; Rajiv Gupta 📵 ;
Masami Ando 📵

🄡 Check for updates

🌐 View Online   📤 Export Citation   CrossMark

Articles You May Be Interested In

Three-dimensional reconstruction of human nipple using refraction-contrast x-ray computed Tomography

AIP Conference Proceedings (January 2019)

2D and 3D Refraction Based X-ray Imaging Suitable for Clinical and Pathological Diagnosis

AIP Conference Proceedings (January 2007)

Growth and characterization of single crystal rocksalt LaAs using LuAs barrier layers

Appl. Phys. Lett. (November 2012)

AIP Publishing

Superimposed wavefront imaging of diffraction-enhanced x-rays: A method to achieve higher resolution in crystal analyzer-based x-ray phase-contrast imaging

Naoki Sunaguchi,[1,a)] (iD) Tetsuya Yuasa,[2] (iD) Daisuke Shimao,[3] (iD) Shu Ichihara,[4] (iD) Rajiv Gupta,[5] (iD) and Masami Ando[6] (iD)

AFFILIATIONS

[1]Department of Radiological and Medical Laboratory Sciences, Nagoya University Graduate School of Medicine, Nagoya, Aichi 461-8673, Japan
[2]Graduate School of Engineering and Science, Yamagata University, Yonezawa, Yamagata 992-8510, Japan
[3]Department of Radiological Technology, Hokkaido University of Science, Sapporo, Hokkaido 006-8585, Japan
[4]Department of Pathology, Nagoya Medical Center, Nagoya, Aichi 460-0001, Japan
[5]Department of Radiology, Massachusetts General Hospital and Harvard Medical School, Boston, Massachusetts 02114, USA
[6]High Energy Accelerator Research Organization, Tsukuba, Ibaraki 305-0801, Japan

[a)]Author to whom correspondence should be addressed: sunaguchi@met.nagoya-u.ac.jp

ABSTRACT

In conventional phase-contrast imaging methods, an optimum distance that is essential for x-ray interference and wavefront separation must be maintained between the object and the x-ray detector. This distance determines the apparent focal size of the x-ray source and affects spatial resolution of the system. To improve the spatial resolution, we proposed a phase-contrast imaging method that eliminates the distance required for x-ray interference and wavefront separation by placing a scintillator in close contact with a Laue angle analyzer (LAA). We mathematically described the image formed by superposition of diffracted beams in two directions of LAA and introduced a method to reconstruct tomographic sections from multiple projections captured by this setup. We experimentally demonstrated the validity and the usefulness of the proposed method. Using a physical phantom, we showed that the proposed method provides higher spatial resolution than conventional x-ray dark-field imaging. The proposed method may be useful for studying and elucidating the fine 3D microanatomy and histopathology of various biological specimens.

Phase-contrast x-ray computed tomography (CT) enables high-contrast visualization of small density differences in biological soft tissues revealing microanatomy that is not amenable to the conventional attenuation-based CT.[1–6] Various imaging techniques have been developed to obtain phase-contrast x-ray CT. These include inline holography,[7] x-ray interferometry,[8] grating-based imaging,[9,10] and analyzer-based imaging.[11–16] All these techniques require an optimum distance—the so-called object to image receptor distance or OID—between the object being imaged and the x-ray detector. For example, inline holography and x-ray grating-based methods use a theoretically calculated OID to form an interference image in space. Similarly, analyzer-based methods use a crystal analyzer—either a Laue-type or Bragg-type single silicon crystal, known as the x-ray dark field imaging

(XDFI), or the diffraction enhanced imaging (DEI), respectively, to obtain phase information. To extract the phase information using these setups, a minimum OID is required. When the distance between the x-ray source and the object is sufficiently long, the OID and the spot size of the x-ray source affect the spatial resolution of the system. A shorter OID makes the apparent focal spot size of the x-ray source smaller, resulting in higher spatial resolution.

In conventional absorption-contrast micro-CT, sub-micron spatial resolution has been demonstrated by minimizing the OID. Using a fourth-generation synchrotron radiation x-ray source with a small spot size and high flux, inline holography has recently been demonstrated to obtain high-spatial resolution phase-contrast x-ray CT of brain and other tissue samples with a spatial resolution of approximately 10 μm.[17]

However, in order to obtain even higher spatial resolution and to achieve high contrast resolution similar to that obtained with crystal optics, it is necessary to reduce the OID to dimensions similar to a micro-CT in an analyzer-based x-ray phase-contrast imaging setup.

In this study, we propose a phase-contrast CT imaging method, namely, superimposed wavefront imaging of diffraction-enhanced x rays (SWIDeX). The optical setup in SWIDeX utilizes a Laue angle analyzer (LAA) made of a single silicon crystal with a scintillator screen that is placed in contact with the exiting face of the LAA. As a result, the x-ray image on the scintillator is formed by superposition of forward diffracted (FD) and diffracted (D) wavefronts. Our optical setup dramatically shortened the OID distance.

We mathematically describe the refraction-contrast projection image of an object formed by the superposition of x-ray wavefronts immediately after they exit from the LAA. Using our mathematical derivation of the combined wavefronts, one can reconstruct tomographic slices through an object from multiple, angularly spaced projections. We experimentally demonstrate the effectiveness of SWIDeX using a physical phantom.

Figure 1 schematically shows the x-ray imaging setup in the analyzer-based method and the proposed SWIDeX method. A parallel x-ray beam incident on the LAA near the Bragg angle θ_B split into FD wavefront traveling in the incident beam direction and D wavefront traveling in a $2\theta_B$ separated from the incident direction. The x-ray intensity in FD and D, as a function of the beam incidence angle to the LAA, follows a rocking curve that can be theoretically calculated. The rocking curve describes the intensity of FD and D in terms of parameters, such as the diffraction plane of the LAA, x-ray energy, and thickness of the LAA. When the x-ray beam enters the LAA at the Bragg angle, the condition where the FD intensity is zero is specifically called the x-ray dark field condition, which forms a steep slope of the rocking curve within the angular range of about 10^{-7} radian near θ_B. The sharp gradient of the rocking curve converts minute changes in the refraction angle generated by an object into significantly large changes in the intensity of FD and D.
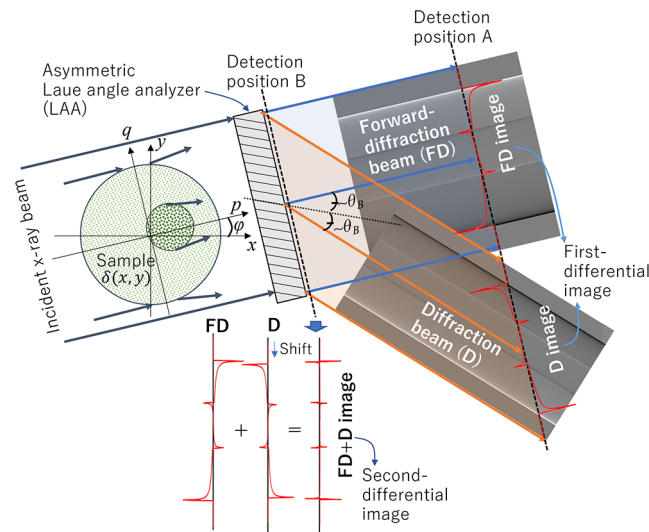

FIG. 1. Overall view of the x-ray imaging in the analyzer-based method and the proposed method.

In conventional XDFI using the LAA with the x-ray dark field condition, the distance between the LAA and the detector needs to be sufficiently large so that FD and D images do not overlap. This position is denoted by the detector position A in Fig. 1. In SWIDeX, we reconstruct CT images of an object from projection images obtained at the detector position B where FD and D wavefronts considerably overlap. For this purpose, we mathematically describe the relationship between the projection image at the position B and the Radon transform of the refractive index distribution of the object.

Consider a pq-coordinate system rotated by φ around the origin of the xy-coordinate system fixed to the object, as shown in Fig. 1. The beam travels parallel to the p-axis and enters the LAA at an angle of θ_0. The detector is placed parallel to the q-axis. The Radon transform of the Laplacian $\Delta\delta(x, y)$ of the refractive index distribution $\delta(x, y)$ at the projection angle φ can be expressed as follows:[18]

$$\int_{-\infty}^{\infty} \Delta\delta(p\cos\varphi - q\sin\varphi, p\sin\varphi + q\cos\varphi)dp$$
$$= \int_{-\infty}^{\infty} \left(\frac{\partial^2}{\partial x^2} + \frac{\partial^2}{\partial y^2}\right)\delta dp = \int_{-\infty}^{\infty} \left(\frac{\partial^2}{\partial p^2} + \frac{\partial^2}{\partial q^2}\right)\delta dp$$
$$= \int_{-\infty}^{\infty} \frac{\partial^2\delta}{\partial q^2}dp + \left[\frac{\partial\delta}{\partial p}\right]_{-\infty}^{\infty} = \int_{-\infty}^{\infty} \frac{\partial^2\delta}{\partial q^2}dp, \tag{1}$$

where $\delta = 0$ outside the object. The right-hand side of Eq. (1) is a projection image representing the second-order derivative of the refractive index distribution $\delta(x, y)$. Therefore, the Laplacian of the refractive index, $\Delta\delta(x, y)$, can be reconstructed by acquiring the projection while changing the projection angle φ.

The diffraction intensities of FD and D at position B can be defined as follows:

$$I_{FD}(q) = R_{FD}(\theta_0 + \alpha(q)) \cdot I(q), \tag{2}$$

$$I_D(q) = R_D(\theta_0 + \alpha(q)) \cdot I(q), \tag{3}$$

where $\alpha(q)$ is the refraction angle caused by the beam propagating through the sample. R_{FD} and R_D are functions representing the rocking curve for FD and D, respectively. When the LAA thickness is very thin, $R_{FD}(\theta) + R_D(\theta) \cong 1$ due to the energy conservation law. $I(q)$ denotes the x-ray intensity after the beam has been absorbed by the subject. The diffraction intensities of FD and D can be expressed as the product of the absorption and the refraction terms. Although the absorption term can be separated from the diffraction intensity by multiple measurements, to simplify the derivation, we assume that the subject is a pure phase object and $I(q) = I_0$. The angular domain Θ_D, where the rocking curve is monotonic, is used for measurement. Defining $f(\theta) = I_0 R_{FD}(\theta)$ and $g(\theta) = I_0 R_D(\theta)$ in $\theta \in \Theta_D$, Eq. (2), Eq. (3), and the energy conservation law are expressed as $I_{FD}(q) = f(\theta_0 + \alpha(q))$, $I_D(q) = g(\theta_0 + \alpha(q))$, and $f(\theta) + g(\theta) = I_0$. Note that at position B, which is a small distance Δp away from behind the LAA, the signal $I_D(q)$ is translated by $\Delta q = \Delta p\tan2\theta_B$, the signal detected at position B can be defined as follows:

$$M(q) = I_{FD}(q) + I_D(q - \Delta q)$$
$$= f(\theta_0 + \alpha(q)) + g(\theta_0 + \alpha(q - \Delta q))$$
$$= f(\theta_0 + \alpha(q)) - f(\theta_0 + \alpha(q - \Delta q)) + I_0. \tag{4}$$

Expanding on the second term, $f(\theta_0 + \alpha(q - \Delta q)) \cong f(\theta_0 + \alpha(q)) - \frac{df}{d\theta}\frac{d\alpha}{dq}\Delta q$, Eq. (4) becomes

$$M(q) \cong \frac{df}{d\theta}\frac{d\alpha}{dq}\Delta q + I_0 = C\frac{d\alpha}{dq} + I_0, \tag{5}$$

where $C = \Delta q \frac{df}{d\theta}(\theta_0 + \alpha(q))$, which can be regarded as a constant that can be obtained by $\frac{df}{d\theta}(\theta_0 + \alpha(q)) \approx \frac{df}{d\theta}(\theta_0)$. The expansion of Eq. (5) is a first-order approximation; a higher-order approximation may be used to represent the output signal with higher precision. Since the refractive angle $\alpha(q)$ represents the first-order differential projection image,[19] $\alpha(q) = \int_{-\infty}^{\infty}\frac{\partial\delta(p,q)}{\partial q}dp$.

Thus, Eq. (5) can be expressed as

$$M(q) = C\int_{-\infty}^{\infty}\frac{\partial^2\delta(p,q)}{\partial q^2}dp + I_0. \tag{6}$$

Therefore, first-order differential projections are acquired with either XDFI or DEI, whereas second-order differential projections are acquired with SWIDeX. Since C and I_0 are known parameters, we can obtain the Radon transform of $\Delta\delta$ from the projected image $M(q)$ at position B in Eq. (1). Finally, $\delta(x, y)$ is obtained by numerically solving the Poisson equation, $(\partial^2/\partial x^2 + \partial^2/\partial y^2)\delta(x,y) = \tilde{\Delta\delta}(x,y)$, where $\tilde{\Delta\delta}$ is an image reconstructed from projections of Eq. (6), under the Dirichlet condition, $\delta(x,y) = 0$ for $(x,y) \in \partial\Omega$. Our implementation employs the successive over-relaxed (SOR) method as a solver.[20]

We constructed an x-ray imaging setup based SWIDeX at the BL14B beamline equipped with a vertical wiggler, high energy accelerator research organization photon factory (KEK-PF), a synchrotron radiation facility in Tsukuba, Ibaraki, Japan. Figure 2 shows a schematic diagram of our CT measurement system based on SWIDeX.

In our imaging setup, the synchrotron radiation x-ray beam obtained from the vertical wiggler was converted to the monochromatic beam at 19.8 keV by a double-crystal monochromator with a Bragg-case Si(111) crystal (not shown in Fig. 2). This beam diffracted at the surface of a monochromatic collimator (MC), an asymmetrically cut Bragg-case Si(111) single crystal. The asymmetry angle of MC, denoted by α_{MC}, was 5.4°. At a Bragg angle θ_B of 5.73°, this asymmetrically cut MC expanded the beam width by a factor of $\frac{1}{b} = \frac{\sin(\theta_B + \alpha_{MC})}{\sin(\theta_B - \alpha_{MC})} \approx 33.5$ fold due to the asymmetric diffraction effect of the MC.

The expanded beam propagated through the sample, after passing through an acrylic filter with a cylindrical hole in the middle. The shape and size of this hole were matched to the cylindrical acrylic rod holding the sample. The acrylic filter has the effects of nulling out the
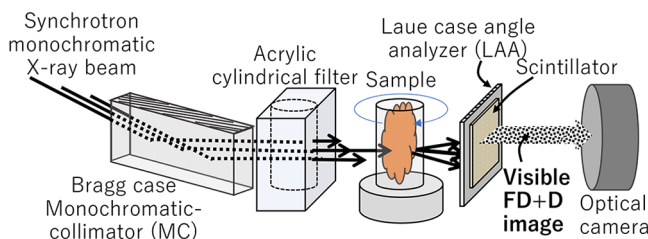

FIG. 2. A schematic diagram of the CT measurement system based on SWIDeX.

absorption-contrast of the cylindrical container and reducing undesired refractive contrast generated on the surface of the cylindrical container. The transmitted beam through the sample was incident on the LAA with a (111) diffraction plane of Si. The LAA had a thickness of 166 μm and an asymmetry angle α_{LAA} of 5°. The angle of incidence of the beam on the LAA surface was $(\theta_B - \alpha_{LAA} - 0.5)$ or approximately 0.73°. Note that the thin LAA is prone to distortion; if the LAA is distorted, the field of view created by diffraction of LAA is non-uniform. To reduce distortion, the LAA was mounted on a mirror-polished 5 mm thick silicon plate, which was perforated only where the beam passes through.

A LuAG:Ce scintillator with a thickness of 100 μm was placed in close proximity of the exiting face of the LAA. The visible image formation by the superposition of FD and D was recorded by an optical camera with a pixel size of 1.55 μm and a matrix size of 4608×2692 pixels. The distance between the rotation axis of the subject and the LAA was approximately 25 mm. Although it was possible to reduce this distance to the maximum radius of the sample, the margin was set to ensure a working distance for mounting the sample in this experiment. The smaller this margin, the smaller the apparent focal size. A total of 2500 angular projections—by incrementally rotating the sample by an angular step of 0.144° around 360°—were acquired for CT reconstruction. The exposure time for each projection image was 4 s, and the total measurement time of the sample was approximately 3 h. The parameter C in Eq. (5) was calculated from the slope in the rocking curve of the LAA obtained from actual measurements. After reconstructing a Laplacian CT image by the filtered backprojection method, a CT image of δ was obtained by the SOR method.

The physical phantom was composed of a 100% carbon fiber felt with a thickness of approximately 20 μm. The carbon fiber felt was placed adjacent to an acrylic rod with a diameter of 1.5 mm. The carbon fiber felt and the acrylic rod were suspended in 1% agarose gel inside a cylindrical PMMA container with an outer diameter of 12 mm and an inner diameter of 10 mm.

Figure 3(a) shows a projection image of the phantom using SWIDeX, depicting the edges of the acrylic rod and the fine fiber structure of the carbon felt. These edges in the image, which represent the second-order derivative of the object as in Eq. (6), were generated by slight displacement and overlap of the FD and D wavefronts. A flat region in the image denotes lack of x-ray refraction in the object. Figure 3(b) shows the line profile of the signal along the green line segment in Fig. 3(a) (the orange curve). This experimentally acquired signal intensity was compared with the theoretical second-order differential of the profile at the edge of the cylinder (the blue curve). The position of the horizontal axis for both profiles was aligned with the minimum intensity of each profile, and the vertical axes of both profiles were normalized so that the minimum intensity of each profile is -1. As can be seen, the position of the maximum value in the measurement profile was shifted to the right from that in the theoretical profile and the shape of the peak intensity in the measured profile was blurred throughout. These effects were caused by misalignment and blurring of FD and D because of multiple diffraction of the x-ray beam inside the LAA and blurring by the thickness of the scintillator. These effects can be decreased by decreasing the thickness of the LAA and the scintillator.

For comparison purposes, we constructed the imaging setup for a conventional XDFI system by modifying the SWIDX optical setup.
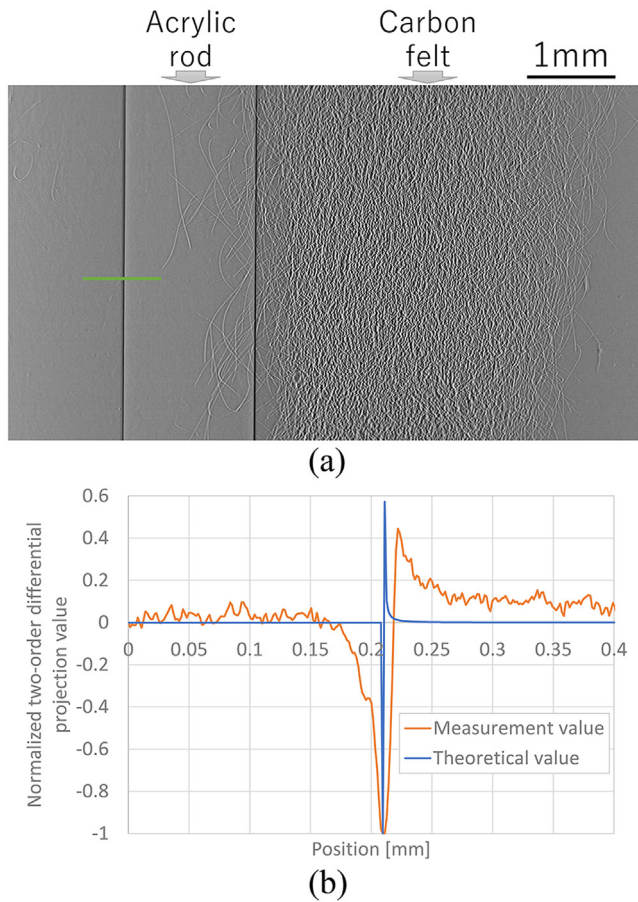
FIG. 3. (a) Projection image of a physical phantom obtained using SWIDeX. (b) The signal intensity along the green line segment in (a). The orange curve shows the experimentally measured signal, and the blue curve shows the theoretical second-order differential profile at the edge of the cylinder.

This modification simply entailed moving the scintillator and optical camera of the SWIDeX setup (Fig. 2) downstream by +380 mm. Such a displacement ensured that FD and D images do not overlap on the scintillator.

Figure 4 shows the reconstructed CT images of $\Delta\delta$ by the proposed SWIDeX method (a), δ by applying the SOR method to the SWIDeX projection images (b), and δ by conventional refraction-contrast CT imaging based on XDFI (c). Figures 4(d), 4(e), and 4(f) are enlarged images corresponding to the yellow square region in Figs. 4(a), 4(b), and 4(c), respectively.

The Laplacian image in Fig. 4(a) showed the fine edge structure of an acrylic rod and carbon fibers with high contrast. A point-like pattern of carbon fibers in the CT image indicated that the fibers extend in a direction orthogonal to the image plane. Figures 4(b) and 4(c) both represent the distribution of δ in the physical phantom. These images clearly showed a density difference between the gel and the carbon fiber or acrylic rod. As can be seen in enlargements of the carbon fiber structures [Figs. 4(d)–4(f)], the image obtained from the proposed method had higher spatial resolution compared with XDFI,

because the OID of SWIDeX was approximately one sixteenth of that from XDFI.

Figure 5 shows the difference line profiles on the yellow line in Figs. 4(b) and 4(c). Each value on each profile was normalized by a 1–0 value. The full width at half maxima in curves of SWIDeX and XDFI was approximately 19 and 28 μm, respectively, and these values represent the magnitude of the blur on the image.

This study demonstrated improved spatial resolution in refraction-contrast CT using the proposed SWIDeX optical setup. In our previous studies, we have demonstrated XDFI-CT for 3D visualization of ductal carcinoma *in situ* (DCIS) in a tissue block from human breasts. XDFI was able to precisely depict the glandular and luminal structures of the milk ducts and associated breast parenchyma in DCIS. XDFI was able to delineate structures with about 20 μm size. However, it failed to delineate the shape of the cellular nuclei which are about 5 μm in diameter. Both glandular architecture and cellular morphology are essential for differentiating different types of cancer for a diagnosis. However, XDFI-CT does not currently have sufficient spatial resolution to delineate them.

To increase the spatial resolution with XDFI, it is necessary to (1) make the LAA thinner and (2) decrease the distance between the LAA and the detector. In the conventional XDFI optical setup, bringing the detector closer to the LAA would reduce the field of view to ensure that the FD and D images do not overlap. The SWIDeX setup overcomes this limitation and essentially eliminates the distance between the object and the detector, making the overall OID like that in micro-CT. As a result, it can achieve higher spatial resolution than XDFI and has the potential to visualize finer morphological details, such as cellular nuclei. It can also achieve a wider field of view. As a limitation of SWIDeX, while XDFI could simultaneously estimate refraction-contrast and absorption-contrast with a single shot of the object by measuring the D image with another camera, SWIDeX requires another shot under conditions where the LAA is rotated several tens of angular seconds from the Bragg angle in order to obtain absorption-contrast.

Unlike other phase-contrast CT imaging techniques that use differential optics, SWIDeX can directly reconstruct a Laplacian image from the acquired projection without using image processing filters. The Laplacian image is useful in observing the contours of complex tissue structures. It can also be used directly as an input image in processing pipelines built for structure extraction and annotation. The Laplacian images, being a second-order differential images, have high sparsity. This feature may be used as a constraint in compressed sensing and machine learning using fewer number of projections required for CT reconstruction, and reconstruction methods using normalization of the total variation and the L1 norm have been proposed.[21,22] We have previously used total variation normalization for phase-contrast based Laplacian CT image reconstruction and were able to reduce the number of projections by a factor of three.[23] Sparsity may also be useful in super-resolution techniques.[24]

In the future, we plan to reduce the thickness of the LAA used for SWIDeX by an order of magnitude (i.e., several tens of μm) to develop an imaging system with a spatial resolution of approximately 1 μm. We will also apply the SWIDeX method to study and elucidate the fine 3D microanatomy and histopathology of various biological specimens.
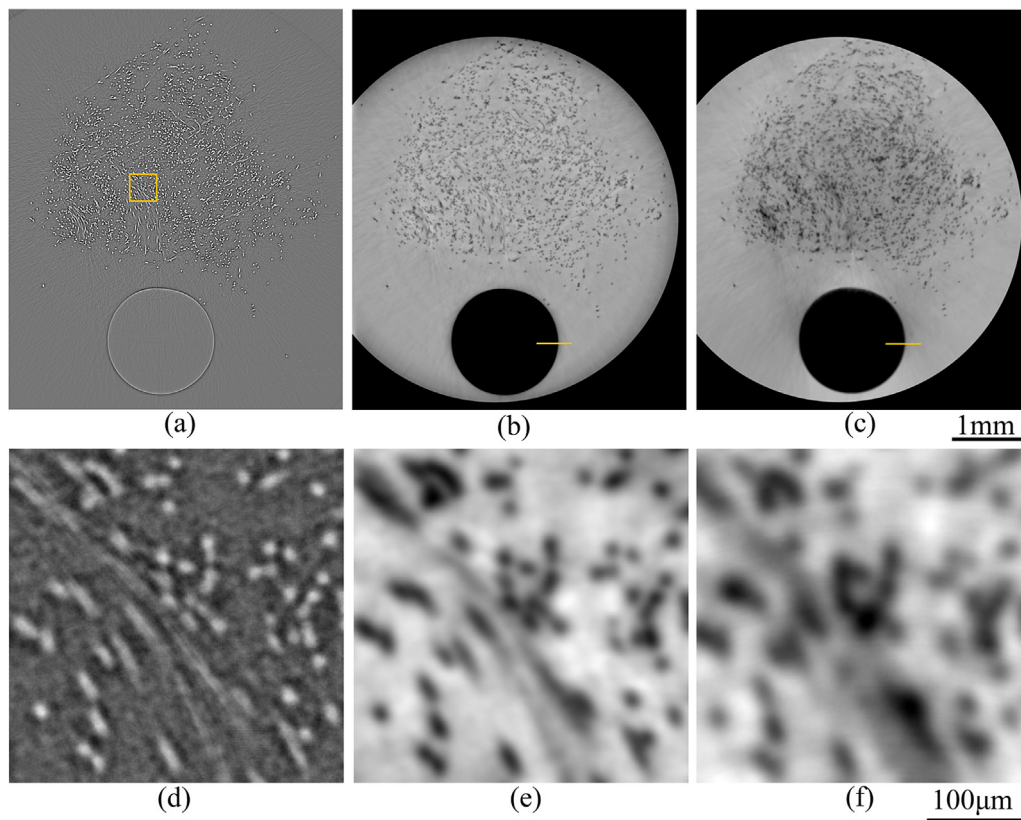
FIG. 4. Comparison of refraction-contrast CT images obtained from the XDFI method and the proposed method. (a) Laplacian CT image by the proposed method, (b) CT image by the proposed method, (c) XDFI-CT image; and (d)–(f) depict an enlarged image of the square area of (a) and enlargement of the corresponding areas in (b) and (c).
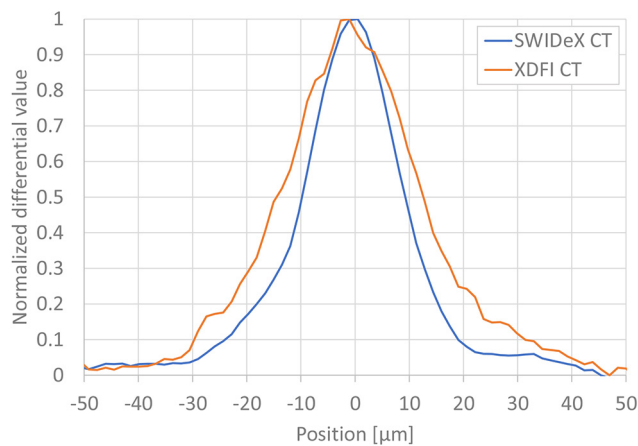

FIG. 5. Difference line profiles on the yellow line in Figs. 4(b) and 4(c).

The experiments were performed as part of five research projects (2008S2002, 2012G562, 2015G597, 2016G0625, 2019G598, and 2020G583) funded by KEK. This research was partially supported by a Grant-in-Aid for Scientific Research (Grant Nos. 16K01369, 15H01129, 26286079, 18K13765, and 21K04077) from

AUTHOR DECLARATIONS
Conflict of Interest

The authors have no conflicts to disclose.

Author Contributions

Naoki Sunaguchi: Conceptualization (lead); Data curation (lead); Formal analysis (lead); Funding acquisition (lead); Investigation (lead); Methodology (lead); Project administration (lead); Resources (lead); Software (lead); Supervision (lead); Validation (lead); Visualization (lead); Writing – original draft (lead); Writing – review & editing (lead). **Tetsuya Yuasa:** Methodology (equal); Validation (supporting); Writing – review & editing (supporting). **Daisuke Shimao:** Data curation (supporting); Writing – review & editing (supporting). **Shu Ichihara:** Writing – review & editing (supporting). **Rajiv Gupta:** Writing – review & editing (equal). **Masami Ando:** Conceptualization

(supporting); Validation (supporting); Writing – review & editing (supporting).

DATA AVAILABILITY

The data that support the findings of this study are available within the article.

REFERENCES

[1] M. Saccomano, J. Albers, G. Tromba, M. Dobrivojević Radmilović, S. Gajović, F. Alves, and C. Dullin, J. Synchrotron Radiat. **25**, 1153 (2018).

[2] G. E. Barbone, A. Bravin, A. Mittone, S. Grosu, J. Ricke, G. Cavaletti, V. Djonov, and P. Coan, Radiology **298**, 135 (2021).

[3] M. Reichardt, M. Töpperwien, A. Khan, F. Alves, and T. Salditt, J. Med. Imaging **7**, 023501 (2020).

[4] M. Ando, N. Sunaguchi, D. Shimao, A. Pan, T. Yuasa, K. Mori, Y. Suzuki, G. Jin, J. Kim, J. Lim, S. Seo, S. Ichihara, N. Ohura, and R. Gupta, Phys. Med. **32**, 1801 (2016).

[5] N. Sunaguchi, D. Shimao, T. Yuasa, S. Ichihara, R. Nishimura, R. Oshima, A. Watanabe, K. Niwa, and M. Ando, Breast Cancer Res. Treat. **180**, 397 (2020).

[6] S. Fujii, T. Muranaka, J. Matsubayashi, S. Yamada, A. Yoneyama, and T. Takakuwa, J. Anat. **237**, 311 (2020).

[7] A. Snigirev, I. Snigireva, V. Kohn, S. Kuznetsov, and I. Schelokov, Rev. Sci. Instrum. **66**, 5486 (1995).

[8] A. Momose, T. Takeda, Y. Itai, and K. Hirano, Nat. Med. **2**, 473 (1996).

[9] A. Momose, S. Kawamoto, I. Koyama, Y. Hamaishi, K. Takai, and Y. Suzuki, Jpn. J. Appl. Phys., Part 1 **42**, L866 (2003).

[10] F. Pfeiffer, T. Weitkamp, O. Bunk, and C. David, Nat. Phys. **2**, 258 (2006).

[11] D. Chapman, W. Thomlinson, F. Arfelli, N. Gm'ur, Z. Zhong, R. Menk, R. E. Johnson, D. Washburn, E. Pisano, and D. Sayers, Rev. Sci. Instrum. **67**, 3360 (1996).

[12] D. Chapman, W. Thomlinson, R. E. Johnston, D. Washbum, E. Pissano, N. Gmur, Z. Zhong, R. Menk, F. Arfelli, and D. Sayers, Phys. Med. Biol. **42**, 2015 (1997).

[13] P. Suortti, J. Keyrilainen, and W. Thomlinson, J. Phys. D **46**, 494002 (2013).

[14] M. J. Kitchen, K. M. Pavlov, S. B. Hooper, D. J. Vine, K. K. W. Siu, M. J. Wallace, M. L. L. Siew, N. Yagi, K. Uesugi, and R. A. Lewis, Eur. J. Radiol. **68**, S49 (2008).

[15] M. Ando, A. Maksimenko, H. Sugiyama, W. Pattanasiriwissawa, K. Hyodo, and C. Uyama, Jpn. J. Appl. Phys., Part 2 **41**, L1016 (2002).

[16] N. Sunaguchi, T. Yuasa, Q. Huo, S. Ichihara, and M. Ando, Appl. Phys. Lett. **97**, 153701 (2010).

[17] C. L. Walsh, P. Tafforeau, W. L. Wagner, D. J. Jafree, A. Bellier, C. Werlein, M. P. Kühnel, E. Boller, S. Walker-Samuel, J. L. Robertus, D. A. Long, J. Jacob, S. Marussi, E. Brown, N. Holroyd, D. D. Jonigk, M. Ackermann, and P. D. Lee, Nat. Methods **18**, 1532 (2021).

[18] A. G. Ramm and A. I. Katsecich, *The Radon Transform and Local Tomography* (CRC Press, 1996).

[19] T. Yuasa, E. Hashimoto, A. Maksimenko, H. Sugiyama, Y. Arai, D. Shimao, S. Ichihara, and M. Ando, Nucl. Instrum. Methods Phys. Res., Sect. A **591**, 546 (2008).

[20] W. H. Press, S. A. Teukolsky, W. T. Vetterling, and B. P. Flannery, *Numerical Recipes in C*, 2nd ed. (Cambridge University, 1992).

[21] G. H. Chen, J. Tang, and S. Leng, Med. Phys. **35**, 660 (2008).

[22] B. Amir and M. Teboulle, SIAM J. Imaging Sci. **2**, 183–202 (2009).

[23] N. Sunaguchi, T. Yuasa, R. Gupta, and M. Ando, Appl. Phys. Lett. **107**, 253701 (2015).

[24] V. Katkovnik, I. Shevkunov, N. V. Petrov, and K. Egiazarian, Optica **4**, 786–794 (2017).